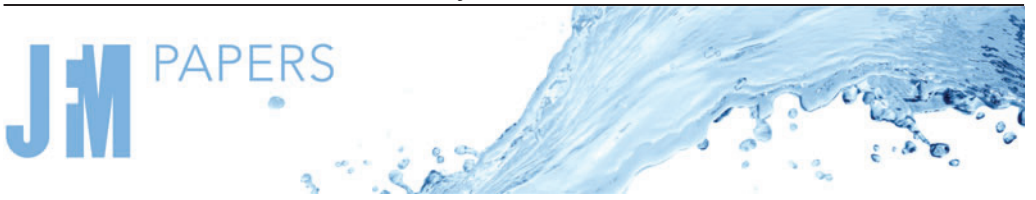
J. Fluid Mech. (2022), *vol*. 948, A49, doi:10.1017/jfm.2022.725



Dewetting acceleration by evaporation

Xiaolong Zhang[1] **and Vadim S. Nikolayev**[1],†

[1]Service de Physique de l'Etat Condensé, CEA, CNRS, Université Paris-Saclay, 91191 Gif-sur-Yvette Cedex, France

(Received 31 March 2022; revised 30 June 2022; accepted 11 August 2022)

Dewetting of a substrate, i.e. the liquid film retraction under partial wetting conditions, has been studied extensively over the past decades. This theoretical work deals with the dewetting phenomenon in the presence of liquid evaporation into the pure vapour atmosphere driven by substrate superheating with respect to the saturation temperature corresponding to the vapour pressure. The dynamic profile of the vapour–liquid interface is analysed numerically by using the generalised lubrication approximation that can be applied to an interface slope larger than its conventional counterpart. This approximation uses a phenomenological argument to increase the precision of calculations. For small slopes, it reduces to the conventional lubrication approach. Several nanoscale effects are included in the theory to obtain more precise results: the Kelvin effect, the hydrodynamic slip, the Marangoni effect, the vapour recoil and the interfacial thermal resistance. Their relative importance is discussed. The results include the film shape evolution, the apparent contact angle and the contact line speed, all defined by the substrate superheating and its wetting properties. These dependencies agree with existing experimental results. It is found that the dewetting is accelerated by evaporation. The numerical results are compared to those of the multiscale theory that uses two main parameters, the Voinov angle (the apparent angle obtained within the microregion problem) and the Voinov length. The latter is studied for several fluids as a function of superheating, and an approximate expression for it is proposed. A good agreement between the numerics and the multiscale theory shows the validity of the latter. This means that the dewetting speed in the presence of evaporation can be calculated with an analytical expression that requires only the Voinov angle as a numerical input. Such results are important for many applications, for instance, bubble growth in boiling or film dynamics in heat pipes.

Key words: contact lines, lubrication theory, condensation/evaporation

† Email address for correspondence: vadim.nikolayev@cea.fr

© The Author(s), 2022. Published by Cambridge University Press

https://doi.org/10.1017/jfm.2022.725 Published online by Cambridge University Press

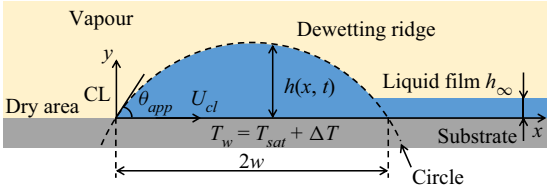


Figure 1. Dewetting ridge receding over a liquid film while the dry area expands.

1. Introduction

Dewetting refers to liquid film retraction from a solid surface previously covered by the liquid. It is a ubiquitous phenomenon that can be observed on a daily basis and is involved in a myriad of industrial applications (de Gennes, Brochard-Wyart & Quéré 2004; Snoeijer & Andreotti 2013). Understanding the dynamics of the contact line (CL) that separates the wetted and dry areas is fundamental to the dewetting dynamics.

We begin with the classical example of dewetting under adiabatic conditions (in the absence of any overall heat and mass transfer between liquid, solid and ambient gas). Consider a smooth solid substrate initially covered by a thick (at least micrometric) liquid film of viscous fluid. Such a film is metastable under partial wetting conditions because once a dry hole is created in the film (i.e. the CL appears), the dry area will grow spontaneously. The motion is driven by the capillary forces. As the CL expands outwards, the film collects the liquid situated previously on the dried area. Due to the high viscous friction in the thin film, this liquid cannot flow inside the film. It thus forms a growing ridge that situates along the CL. One can take the vertical cross-section that passes through the centre of a dry hole. The problem is then described in two dimensions, as shown in figure 1. Experimental studies have shown that the CL recedes at a constant speed (Brochard-Wyart *et al.* 1991; de Gennes *et al.* 2004; Edwards *et al.* 2016). Conversely, the theoretical analysis by Snoeijer & Eggers (2010) has shown that the receding speed U_{cl} should decline very slowly (logarithmically) with time (or with the ridge size w that grows with time).

Previous dewetting studies concern mainly the adiabatic conditions. However, thin film flows are used extensively in industrial applications where the film evaporation/condensation is employed as a highly efficient mean of heat transfer. Applications include such classical cooling devices as falling film chillers or heat pipes. More recently, dewetting was studied in the context of pulsating heat pipes (Nikolayev 2021) and bubble growth in boiling (Urbano *et al.* 2018; Bureš & Sato 2021).

In all these applications, the phase change occurs simultaneously with dewetting; the liquid film is surrounded by the pure vapour of the same fluid. In this work, we continue the line of thought put forward in our previous paper (Zhang & Nikolayev 2021), where the lubrication approximation was used to describe the thin film flow. The objectives of this work are threefold. The primary aim is to find the numerical solution to the dewetting problem in the presence of liquid film evaporation created by the heated substrate. For this, one needs to discuss first (§ 2.2) the nanoscale effects relevant to the description of CL vicinity, where the evaporation is extreme. As the slope of the liquid–vapour interface increases in the presence of evaporation, the conventional lubrication approach becomes insufficient. We thus develop the generalised lubrication theory suitable for larger interface slopes. Another objective of this paper is to generalise to the case of evaporation the multiscale theory proposed initially by Snoeijer & Eggers (2010) for adiabatic dewetting (§ 2.3). The main parameters of the multiscale theory are discussed, and its results are

https://doi.org/10.1017/jfm.2022.725 Published online by Cambridge University Press

compared to the numerical solution. The dependence of CL receding speed on the heating rate is discussed. Finally, the numerical results are compared to the experiment in § 3.5.

2. Problem formulation

We start with the conventional lubrication equations and then progressively add extra terms to them that lead to the formulation used for the computations.

2.1. *Conventional lubrication equations*

Consider the dewetting problem shown in figure 1, where the liquid film of thickness h_∞ is surrounded by the pure vapour of the same substance. Since the vapour density ρ_v, viscosity and thermal conductivity are all small compared to the liquid, one can apply the 'one-sided' formulation where both the vapour-side hydrodynamic stress and the heat flux into the vapour at the interface are neglected in comparison with values on the liquid side. Therefore, the vapour pressure p_v is assumed to be spatially homogeneous. The substrate is assumed to be highly conductive and thus isothermal. The wall temperature $T_w = T_{sat} + \Delta T$ can differ from $T_{sat} = T_{sat}(p_v)$, thus causing the film evaporation or condensation for positive or negative ΔT, respectively.

To begin with, one formulates the dewetting problem by using the conventional lubrication theory in two dimensions (x, y), where the interface is described as $y = h(x, t)$. In the frame of reference of the CL that recedes with the speed U_{cl}, the governing equation reads (Zhang & Nikolayev 2021)

$$\frac{\partial h}{\partial t} + \frac{\partial}{\partial x}\left(\frac{h^3}{3\mu}\frac{\partial \Delta p}{\partial x} - U_{cl}h\right) = -\frac{J}{\rho_l}, \tag{2.1}$$

where J (assumed positive for evaporation) is the mass flux at the interface, and μ and ρ_l are the liquid shear viscosity and density, respectively. In this frame of reference, the transient term $\partial h/\partial t$ describes a slow dewetting ridge growth.

A quasi-stationary linear temperature profile is assumed along the y axis. The interfacial energy balance results in

$$J = \frac{k(T_w - T^i)}{h\mathcal{L}}, \tag{2.2}$$

where T^i is the temperature of the vapour–liquid interface, k is the liquid heat conductivity, and $\mathcal{L}$ is the latent heat.

The pressure jump $\Delta p \equiv p_v - p_l$ across the vapour–liquid interface satisfies the Laplace equation

$$\Delta p = \sigma K, \tag{2.3}$$

where σ is the surface tension, and the interface curvature is

$$K \simeq \frac{\partial^2 h}{\partial x^2} \tag{2.4}$$

in the small-slope approximation.

2.2. *Relaxing the singularity at the contact line*

Even for the adiabatic case (i.e. for $\Delta T = 0$), the conventional hydrodynamic description of the moving CL leads to the viscous dissipation divergence at the CL where $h \to 0$

https://doi.org/10.1017/jfm.2022.725 Published online by Cambridge University Press

(de Gennes 1985). Wayner (1993) was the first to hypothesise that this singularity can be relaxed for volatile fluids through evaporation/condensation when it matches CL displacement. Rather than sliding over the solid, the CL recedes because liquid on it evaporates, or advances by liquid condensation. It turns out to be possible thanks to the Kelvin effect. The Kelvin effect provides the variation of T^i along a curved interface:

$$T^i = T_{sat}\left(1 + \frac{\Delta p}{\mathcal{L}\rho_l}\right). \tag{2.5}$$

The interface is strongly curved near the CL to agree with the phase change rate, which, in turn, is regulated by CL motion. Within such a description, Janeček & Nikolayev (2012) have shown that the liquid pressure remains finite at the CL, thus the singularity is relaxed. Janeček *et al.* (2013) and Rednikov & Colinet (2013) have used asymptotic matching to show that the Kelvin effect is sufficient to describe CL motion in case of volatile fluids.

In the diabatic case ($\Delta T \neq 0$), an additional singularity related to the mass change term J appears in (2.1). Indeed, if the Kelvin effect was neglected, then $T_w - T^i$ would be constant ($= \Delta T$), and the mass flux (2.2) would diverge as $h \to 0$. The Kelvin effect relaxes the singularity in this case too. One notes that the singularity relaxation can be achieved even without accounting for the Kelvin effect. The moving CL singularity can be regularised by introducing the hydrodynamic slip at the liquid–solid interface (Hocking 1983). However, accounting for an additional nanoscale effect, the interfacial resistance is necessary to regularise the mass flux (Hocking 1995; Saxton *et al.* 2017) in the case where it exists – note the correction (Anderson & Janeček 2018) of the Hocking formula.

2.2.1. *Hydrodynamic slip and interfacial thermal resistance*

The no-slip boundary condition at the liquid–solid interface can be violated when the hydrodynamic stress is very strong. The slip length l_s is introduced to quantify the slip of liquid molecules over the solid; l_s is defined as a distance from the liquid–solid boundary where the linear extrapolation of the tangential component of the liquid velocity $u_x(y)$ vanishes. Using l_s, the Navier slip boundary condition is written as

$$u_x = l_s \frac{\partial u_x}{\partial y}. \tag{2.6}$$

The value of l_s is usually several nanometres but can be one order of value larger for non-wettable surfaces (Lauga, Brenner & Stone 2007). In all our calculations, we assume $l_s = 10\,\text{nm}$, which is the value coherent with the previous works accounting for it (Delon *et al.* 2008; Nikolayev 2010; Janeček & Nikolayev 2012; Fourgeaud *et al.* 2016; Chan *et al.* 2020). With the account of the slip, the governing equation (2.1) becomes

$$\frac{\partial h}{\partial t} + \frac{\partial}{\partial x}\left[\frac{h^2}{3\mu}(h + 3l_s)\frac{\partial \Delta p}{\partial x} - U_{cl}h\right] = -\frac{J}{\rho_l}. \tag{2.7}$$

The interfacial thermal resistance R^i is of importance when the interfacial mass flux J is strong, so the corresponding vapour escape speed is comparable with the thermal velocity of molecules (Nikolayev 2022). It is true at the CL where J is high. The interfacial thermal

https://doi.org/10.1017/jfm.2022.725 Published online by Cambridge University Press

resistance reads

$$R^i = \frac{T_{sat}\sqrt{2\pi R T_{sat}/M}(\rho_l - \rho_v)}{2\mathcal{L}^2\rho_l\rho_v}, \tag{2.8}$$

where R is the universal gas constant, and M is the molar mass. Here, R^i provides an extra term to (2.5):

$$T^i = T_{sat}\left(1 + \frac{\Delta p}{\mathcal{L}\rho_l}\right) + R^i J\mathcal{L}, \tag{2.9}$$

and (2.2) modified by R^i and the Kelvin effect reads

$$J = \frac{\Delta T - \Delta p\, T_{sat}/(\rho_l\mathcal{L})}{\mathcal{L}(R^i + h/k)}. \tag{2.10}$$

Without the Kelvin effect, the account of both R^i and l_s provides a finite J and a logarithmically divergent p_l at the CL. This divergence is integrable, which means that the measurable hydrodynamic stress is finite, so the singularity is relaxed. The introduction of the Kelvin effect leads to a finite pressure at the CL, which is more reasonable from the physical point of view and much more convenient for numerical calculations where a pressure boundary condition can be imposed (see § 2.6) instead of using the numerical matching to asymptotic solutions at $x \to 0$ required in the absence of the Kelvin effect.

In order to obtain results comparable to experimental data, one needs to account for two more effects known to considerably affect the free interface shape in the CL vicinity (see § 2.4): the Marangoni effect and vapour recoil.

2.2.2. *The Marangoni effect*

Since the temperature (2.9) varies along the interface, the corresponding variation of surface tension can be important:

$$\frac{\partial\sigma}{\partial x} \simeq -\gamma\frac{\partial T^i}{\partial x}, \tag{2.11}$$

where $\gamma = -\partial\sigma/\partial T$ is generally positive for pure fluids. Such a variation contributes to the tangential interface stress component (which is referred to as the Marangoni effect). An extra term should be added to (2.7), which becomes (Nikolayev 2010)

$$\frac{\partial h}{\partial t} + \frac{\partial}{\partial x}\left\{\frac{1}{\mu}\left[\frac{h}{2}(h + 2l_s)\frac{\partial\sigma}{\partial x} + \frac{h^2}{3}(h + 3l_s)\frac{\partial\Delta p}{\partial x}\right] - U_{cl}h\right\} = -\frac{J}{\rho_l}. \tag{2.12}$$

Note that the temperature variation occurs only at the nanoscale; at a larger scale, the interfacial temperature is constant.

2.2.3. *Vapour recoil*

The recoil pressure p_r (Nikolayev & Beysens 1999) is created at the liquid–vapour interface by the fluid molecules escaping the interface towards the vapour. This effect modifies the

https://doi.org/10.1017/jfm.2022.725 Published online by Cambridge University Press

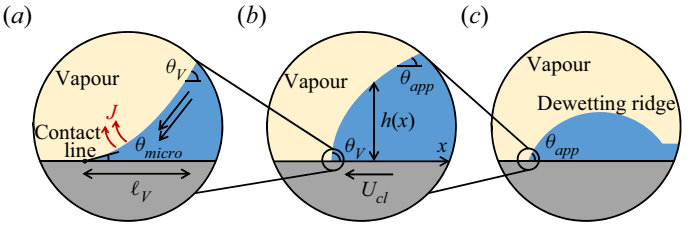


Figure 2. Length scale hierarchy in the case of a moving contact line: (*a*) microscopic region, (*b*) intermediate region, (*c*) macroscopic region.

pressure jump (2.3):

$$\Delta p = \sigma K - p_r, \tag{2.13}$$

where

$$p_r = J^2 \left(\frac{1}{\rho_v} - \frac{1}{\rho_l} \right). \tag{2.14}$$

The vapour recoil also affects the interfacial temperature by providing an additional term to (2.9) (Anderson *et al.* 2007):

$$T^i = T_{sat} \left[1 + \frac{\Delta p}{\mathcal{L}\rho_l} + \frac{J^2}{2\mathcal{L}} \left(\frac{1}{\rho_v^2} - \frac{1}{\rho_l^2} \right) \right] + R^i J \mathcal{L}. \tag{2.15}$$

Together with (2.2), (2.13) and (2.15), (2.12) governs the interface evolution.

2.3. *Multiscale analysis*

Equation (2.12) is complex because it involves several very different length scales. Since these scales generally differ by several orders of magnitude, one can apply the multiscale asymptotic analysis. The governing physical effects at one scale can be neglected at another. For the problem of a moving CL with phase change (Janeček *et al.* 2013), three scales (and the corresponding regions) can be identified (figure 2).

The smallest scale is traditionally referred to as the microregion. Its characteristic size $\ell_V \sim 100\,\text{nm}$ is called hereafter the Voinov length. Its rigorous definition will be given below. In figure 2(*a*), the microregion is illustrated for the partial wetting case with the microscopic contact angle θ_{micro}, which is the actual contact angle at the CL. Within this region, phase change is the dominant phenomenon; the nanoscale effects discussed in § 2.2 are all significant. The flow caused by evaporation is so strong that the impact of CL motion is negligible, so both transient and U_{cl} terms can be neglected in (2.12). At the right-hand boundary of the microregion (far from the CL), the interface slope saturates to a value that we call hereafter the Voinov angle θ_V, which depends on θ_{micro} and ΔT (Janeček & Nikolayev 2012). Intensive evaporation near the CL induces a strong liquid flow towards it, which, together with the vapour recoil (Nikolayev 2022), leads to a strongly curved interface. As a consequence, $\theta_V > \theta_{micro}$. The opposite tendency occurs at condensation. In the adiabatic case ($\Delta T = 0$), $\theta_V = \theta_{micro}$.

The intermediate region (typically between 100 nm and 100 µm from the CL) is dominated by the flow induced by CL motion, so the terms responsible for the evaporation-induced flow (and discussed above nanoscale effects) can all be neglected together with the transient term. The interfacial shape is a result of a balance of the surface

https://doi.org/10.1017/jfm.2022.725 Published online by Cambridge University Press

tension and viscous forces. Such a problem has been investigated by many researchers. Voinov (1976) has derived an asymptotic law that predicts the interface slope ϕ as a function of CL velocity:

$$\phi^3 = \theta^3 - 9\,Ca \ln \frac{x}{\ell_V}, \tag{2.16}$$

where the dimensionless dewetting speed (the capillary number) is $Ca = \mu U_{cl}/\sigma$. It is positive for the CL receding and negative for advancing over the dry area. By considering the corresponding Stokes problem, Cox (1986) showed that its solution can be approximated with (2.16). The approximation remains accurate until a slope as high as 150° (Snoeijer & Andreotti 2013). Two parameters, ℓ_V and θ, should be determined from the asymptotic matching to the microregion solution. As we will see in § 3.2, $\theta = \theta_V$.

One of the main objectives of problems involving the CL is to calculate the apparent contact angle θ_{app}, i.e. the contact angle obtained at the macroscopic scale corresponding to the dewetting ridge size (Snoeijer & Andreotti 2013; Nikolayev 2022). The corresponding region is often called the macroregion. Such a problem is defined by the balance of the transient and surface tension terms in (2.12). Snoeijer & Eggers (2010) considered the adiabatic dewetting problem. They have shown that after initial transients, the macroscopic ridge shape is defined mainly by the surface tension. This means that θ_{app} can be obtained by fitting the ridge shape to a circle (figure 1). With the slip used for the singularity relaxation, Snoeijer & Eggers (2010) have performed the asymptotic matching between the CL region, the macroscopic liquid ridge and the flat film of thickness h_∞ in the adiabatic case. One of their central results is

$$\theta_{app}^3 = \theta_V^3 - 9\,Ca \ln \frac{2w}{e\ell_V}, \tag{2.17}$$

where w is the ridge half-width (figure 1), and $e \simeq 2.71$ is the Euler number. The problem solved by Snoeijer & Eggers (2010) is adiabatic; their ℓ_V is thus equal to

$$\ell_{Vsa} = \frac{3l_s}{e\theta_{micro}}. \tag{2.18}$$

The main result of Snoeijer & Eggers (2010) is the asymptotic expression for the dewetting speed,

$$Ca = \frac{\theta_V^3}{9}\left[\ln\left(\frac{4a}{e^2}\,Ca^{1/3}\,\frac{w^2}{\ell_V h_\infty}\right)\right]^{-1}, \tag{2.19}$$

where $a \simeq 1.094$. As argued by Fourgeaud *et al.* (2016), both expressions above should hold for any microregion model (including that accounting for the evaporation) because of the scale separation. However, one needs to determine the key parameters ℓ_V and θ_V, and verify if (2.17) and (2.19) are indeed valid under the conditions of evaporation. To explain their experimental results, Fourgeaud *et al.* (2016) hypothesised that the liquid mass loss caused by strong evaporation at the CL can accelerate the CL receding, in addition to the capillary effect described by (2.19). This issue needs to be clarified.

2.4. *Relative contributions of different nanoscale effects*

Two main effects that can relax the hydrodynamic CL singularity are the Kelvin effect and the hydrodynamic slip, which together determine ℓ_V. The other effects considered above are generally secondary for ℓ_V but impact θ_V more or less strongly. A contribution

https://doi.org/10.1017/jfm.2022.725 Published online by Cambridge University Press

			Values (nm) for $\Delta T = 5\,\mathrm{K}$					
			FC72		Ethanol		Water	
			$\theta_{micro} = 5^\circ$ $\theta_V = 31.6^\circ$		$\theta_{micro} = 5^\circ$ $\theta_V = 26.1^\circ$		$\theta_{micro} = 10^\circ$ $\theta_V = 18.5^\circ$	
Length	Effect	θ	θ_{micro}	θ_V	θ_{micro}	θ_V	θ_{micro}	θ_V
$\ell_K = \frac{\sqrt{3\mu_l k_l T_{sat}}}{\rho_l \mathcal{L} \theta^2}$	Kelvin		150.7	3.78	64.6	2.36	7.02	2.05
$\ell_s = \frac{3l_s}{\theta}$	Hydrodynamic slip		344	65.7	344	65.7	172	92.9
$\ell_R = \frac{R^i k}{\theta}$	Interfacial resistance		434	69.6	542	102	248	134
$\ell_{MR} = \frac{3\gamma\, \Delta T\, R^i k}{2\theta^3 \sigma}$	Marangoni		3138	12.4	3372	23.7	199.5	31.5
$\ell_r = \frac{\Delta T^2 k^2}{\theta^3 \mathcal{L}^2 \sigma} \left(\frac{1}{\rho_v} - \frac{1}{\rho_l} \right)$	Vapour recoil		234	0.93	152	1.07	12.1	1.91

Table 1. Characteristic length scales of different nanoscale effects.

of an effect to the overall system dynamics can be evaluated by defining the corresponding characteristic length scales. They are defined as a distance from the CL along the x axis at which the effect is still important. An effect overcomes another if its characteristic length is larger. The definitions of these scales presented in table 1 are discussed in Appendix B.

For estimation purposes, one assumes that the liquid forms a straight wedge with the opening angle θ. The above analysis shows, however, that the interface slope grows from θ_{micro} to θ_V in the microregion. Therefore, one can define the bounds for the characteristic lengths only by using these two values for θ.

For all the fluids, the Kelvin length ℓ_K is smaller than the slip characteristic length scale ℓ_s, which means that the slip controls ℓ_V. As the value of ℓ_R is comparable to ℓ_s, the interfacial thermal resistance strongly impacts the Voinov angle. This is valid for all the fluids. The vapour recoil is generally weak, which is not surprising accounting for the low $\Delta T = 5\,\mathrm{K}$ considered in table 1. As its corresponding scale is $\ell_r \sim \Delta T^2$, it exercises a much stronger influence at a higher ΔT. However, this effect is less important for water than for the other two fluids.

One can see that ℓ_{MR} computed at the CL (i.e. with θ_{micro}) can be very large. These large values are, however, only the upper bounds. The impact of the Marangoni effect is extremely strong in the close CL vicinity, but drops very quickly as the slope in the microregion increases towards θ_V at the border of the microregion. This analysis shows that, generally, all of the above nanoscale effects impact CL dynamics, and none of them should be neglected.

2.5. *Generalised lubrication theory*

As the strongest hydrodynamic stresses occur in the CL vicinity, we consider an example of the curved wedge geometry shown in figure 3(*a*). Nevertheless, the approach presented hereafter does not lose its generality for any liquid film geometry.

https://doi.org/10.1017/jfm.2022.725 Published online by Cambridge University Press

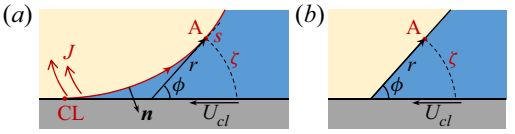


Figure 3. Sketch of (*a*) the curved interface and (*b*) the straight liquid wedge, corresponding to the point A.

High interface slopes can occur in the dewetting problem at evaporation that causes $\theta_V > \theta_{micro}$. When the interface slope ϕ is larger than $\sim 30°$, the conventional lubrication equation (2.12), valid for small slopes, is hardly applicable. In this case, one can take advantage of a more accurate approach suggested initially by Boender, Chesters & van der Zanden (1991) and rediscovered more recently by Snoeijer (2006). Instead of operating with the coordinate x, it uses the parametric interface description in terms of the curvilinear coordinate s that runs along it, with $s = 0$ at the CL. Therefore, the following geometrical relations hold:

$$\frac{\partial h}{\partial s} = \sin\phi, \tag{2.20a}$$

$$\frac{\partial x}{\partial s} = \cos\phi, \tag{2.20b}$$

where ϕ is the local interface slope. The major convenience of such a parametrisation is that instead of the approximation (2.4), one uses the rigorous geometrical curvature definition

$$K = \frac{\partial \phi}{\partial s}. \tag{2.21}$$

Consider an interfacial point A with coordinate s. The approach consists in approximating the tangential pressure gradient $\partial p_l/\partial s$ at A (figure 3*a*) by that created by the flow in a straight liquid wedge, the opening angle of which is ϕ; cf. figure 3(*b*). In other words, if one introduces the polar radius r of the point A defined within the corresponding straight wedge, then this hypothesis reads

$$\frac{\partial p_l}{\partial s} \simeq \frac{\partial p_l}{\partial r}. \tag{2.22}$$

Here, the right-hand side is calculated within the straight wedge problem; the upper ray of the straight wedge (to which A belongs) is tangential to the curved interface, meaning $\partial s = \partial r$.

2.5.1. *Generalised moving contact line description*

This theory was developed initially to describe the adiabatic moving CL problem (at $J = 0$); it was used in many works – see e.g. Delon *et al.* (2008) and Chan *et al.* (2013, 2020). In this case, the pressure gradient is induced by the interface motion (in the reference frame where the wedge is immobile). The Stokes problem (see Appendix A) results in

$$\frac{\partial \Delta p}{\partial s} = \frac{3\mu U_{cl}}{h^2}\bar{F}(\phi), \tag{2.23}$$

where the spatial homogeneity of p_v is assumed and

$$\bar{F}(\phi) = \frac{2}{3}\frac{\sin^3\phi}{\phi - \sin\phi\cos\phi}. \tag{2.24}$$

https://doi.org/10.1017/jfm.2022.725 Published online by Cambridge University Press

One mentions that $\bar{F}(\phi \to 0) = 1$, so the generalised theory reduces to the conventional lubrication approach for small slopes as expected.

Another generalisation is required to include the hydrodynamic slip in the model. The analytical solution to the Stokes problem is not known for this case. In previous works (Delon *et al.* 2008; Chan *et al.* 2013), the slip length was introduced as in the conventional lubrication equation

$$\frac{\partial \Delta p}{\partial s} = \frac{3\mu U_{cl}}{h(h + cl_s)} \bar{F}(\phi) \tag{2.25}$$

with the hypothesis $c = 3$. In a subsequent work (Chan *et al.* 2020), the c coefficient has been found for the specific problem of adiabatic CL dynamics as a function of θ_{micro}: $c = 3 - (9/10)\theta_{micro}^2 + o(\theta_{micro}^2)$. However, in general, c should depend not on the boundary conditions (θ_{micro} is one of them) but on the local interface slope, so the result of Chan *et al.* (2020) cannot be used here directly. We propose the following phenomenological argument that leads to a similar result. In the conventional lubrication equation, the velocity gradient varies linearly along the vertical axis. However, in a wedge geometry, where the flow lines are usually convergent (or divergent), one can reasonably assume that the velocity gradient varies linearly along an arc (which is actually the case in the straight wedge Stokes problem of Appendix A). The arc centre can be defined locally for each interface point A as an intersection of the tangent to the interface with the wall. The arc radius r is the distance from A to the centre (figure 3*a*), with r related to h via

$$h = r \sin \phi. \tag{2.26}$$

The arc length is $\zeta = \phi r$ or

$$\zeta = h\phi / \sin \phi. \tag{2.27}$$

Instead of (2.25), one can thus write

$$\frac{\partial \Delta p}{\partial s} = \frac{3\mu U_{cl}}{\zeta(\zeta + 3l_s)} F(\phi), \tag{2.28}$$

where

$$F(\phi) = \frac{2\phi^2}{3} \frac{\sin \phi}{\phi - \sin \phi \cos \phi} \tag{2.29}$$

satisfies $F(\phi \to 0) = 1$.

Note that (2.28) is equivalent to (2.25) with $c = 3 \sin \phi / \phi = 3 - (1/2)\phi^2 + o(\phi^2)$. Since $\phi \to \theta_{micro}$ near the CL, this expression is quite close to the above result of Chan *et al.* (2020) but has the advantage of being usable universally. On the basis of the above argument, such a 'ζ-formulation' will be used hereafter for all other terms.

2.5.2. *Generalised description including the phase exchange*

Mathieu (2003) proposed the generalised description of the phase exchange. His approach is based on its strong localisation near the CL. The Stokes problem (§ A.2) assumes that the mass exchange is modelled by a point source Φ localised at the CL. Here, Φ is defined as a flux through the arc of the length ζ (figure 3):

$$\Phi = \int_0^{\phi} r\, u_r \, \mathrm{d}\varphi, \tag{2.30}$$

where u_r is the component of the liquid velocity $\boldsymbol{u}$ assumed to be normal to the arc.

https://doi.org/10.1017/jfm.2022.725 Published online by Cambridge University Press

For the $\partial p_l/\partial s$ definition, this model assumes that the flow along the interface at a point with the coordinate s (figure 3*a*) is provided by a source located at a smaller s (i.e. closer to the CL) (Janeček & Nikolayev 2014). Evidently, when the phase exchange is distributed over the interface, $\Phi = \Phi(s)$. This assumption results in

$$\frac{\partial \Delta p}{\partial s} = \frac{3\mu\Phi}{\zeta^2(\zeta + 3l_s)}\, G(\phi), \tag{2.31}$$

where

$$G(\phi) = \frac{\phi^3}{3}\,\frac{4}{\sin\phi\cos\phi - \phi\cos 2\phi} \tag{2.32}$$

is the correction factor to the conventional lubrication theory (2.12), $G(\phi \to 0) = 1$. The slip length is introduced here similarly to (2.28).

To include both sources of the liquid flow along the wedge, i.e. CL motion and the phase exchange, one can take advantage of the linearity of the Stokes equations. The total pressure drop is thus a sum

$$\frac{\partial \Delta p}{\partial s} = \frac{3\mu[\Phi\, G(\phi) + \zeta\, U_{cl}\, F(\phi)]}{\zeta^2(\zeta + 3l_s)} \tag{2.33}$$

of the contributions (2.28) and (2.31).

One more assumption concerns the Marangoni term. By using the 'ζ-formulation' for it, one can write in an analogy with (2.12):

$$\mu[\Phi\, G(\phi) + \zeta\, U_{cl}\, F(\phi)] = \frac{\zeta}{2}\,(\zeta + 2l_s)\,\frac{\partial \sigma}{\partial s} + \frac{\zeta^2}{3}\,(\zeta + 3l_s)\,\frac{\partial \Delta p}{\partial s}. \tag{2.34}$$

Such an ansatz can be justified by the diverging flow in a wedge and by the fact that the Marangoni term is important only in the close vicinity of the CL where the slope remains generally small (of the order of θ_{micro}) in most cases.

By using the liquid volume conservation, Φ can be expressed via the component $u_n = \boldsymbol{u}\cdot\boldsymbol{n}$ of the liquid velocity $\boldsymbol{u}$, which is normal to the vapour–liquid interface (with the vector $\boldsymbol{n}$ directed towards the liquid; see figure 3*a*):

$$\Phi = \int_0^s u_n(s)\,\mathrm{d}s. \tag{2.35}$$

One can rewrite this expression as

$$u_n = \frac{\partial \Phi}{\partial s} \tag{2.36}$$

and make use of the liquid mass conservation at the interface (Nikolayev 2010):

$$J = (u^i - u_n)\rho_l. \tag{2.37}$$

Here, the interface velocity projection to $\boldsymbol{n}$ is

$$u^i = -\frac{\partial h}{\partial t}\cos\phi. \tag{2.38}$$

By eliminating Φ in (2.36) with (2.34) and injecting it into (2.37) together with (2.38), one finally obtains the generalised counterpart of (2.12):

$$\frac{\partial h}{\partial t}\cos\phi + \frac{\partial}{\partial s}\left\{\frac{1}{\mu\, G(\phi)}\left[\frac{\zeta}{2}\,(\zeta + 2l_s)\,\frac{\partial \sigma}{\partial s} + \frac{\zeta^2}{3}\,(\zeta + 3l_s)\,\frac{\partial \Delta p}{\partial s}\right] - U_{cl}\zeta\,\frac{F(\phi)}{G(\phi)}\right\} = -\frac{J}{\rho_l}. \tag{2.39}$$

https://doi.org/10.1017/jfm.2022.725 Published online by Cambridge University Press

Two more equations need to be written to define Δp and J that appear in (2.39). The temperature distribution is assumed to be linear along the arc length ζ (figure 3*a*), as suggested by the rigorous thermal analysis of the straight wedge (Anderson & Davis 1994). Instead of (2.2), one then obtains

$$J = \frac{k(T_w - T^i)}{\zeta \mathcal{L}}, \tag{2.40}$$

where the interface temperature is expressed with (2.15). The pressure jump equation

$$\frac{\sigma}{\cos\phi}\frac{\partial^2 h}{\partial s^2} - \Delta p = J^2\left(\frac{1}{\rho_v} - \frac{1}{\rho_l}\right) \tag{2.41}$$

is a combination of (2.13), (2.14), (2.20*a*) and (2.21).

2.6. *Boundary conditions and contact line receding speed*

The problem is solved for $s \in [0, s_f]$, with s_f a point far from the ridge, where the film can be assumed flat. The film flatness condition (zero spatial derivatives and $\phi = 0$) used in (2.39) results in

$$h_\infty = h_0\sqrt{1 - \frac{t}{t_d}}, \tag{2.42}$$

where h_0 is the initial ($t = 0$) film thickness, and

$$t_d = \frac{\mathcal{L}\rho_l h_0^2}{2k\,\Delta T} \tag{2.43}$$

is the film drying time. For the adiabatic problem ($\Delta T = 0$), the thickness $h_\infty = h_0$ remains constant.

At the CL ($s = 0$), the geometry implies

$$\left.\begin{aligned} h &= 0, \\ \frac{\partial h}{\partial s} &= \sin\theta_{micro}. \end{aligned}\right\} \tag{2.44}$$

The set of lubrication equations (2.39) and (2.41) is of fourth order, so one more boundary condition is required. It should express the regularity of all physical quantities at the CL (their finiteness and continuity). To derive this condition for the generalised lubrication approach, one can proceed similarly to Janeček & Nikolayev (2012), who obtained it for the conventional case. The temperature continuity implies that the interface temperature T^i at the CL should be equal to the temperature of the solid, $T_w = T_{sat} + \Delta T$. From (2.15), one obtains the condition

$$\Delta p = \frac{\mathcal{L}\rho_l}{T_{sat}}(\Delta T - R^i J\mathcal{L}) - \frac{J^2\rho_l}{2}\left(\frac{1}{\rho_v^2} - \frac{1}{\rho_l^2}\right), \tag{2.45}$$

valid asymptotically as $s \to 0$. To obtain $J(s \to 0)$, (2.39) is integrated from 0 to s, where s is infinitesimally small, so $\zeta = s\theta_{micro}$. The regularity of all physical quantities results in

$$-\gamma\frac{\partial T^i}{\partial s} + \theta_{micro}s\frac{\partial \Delta p}{\partial s} = \frac{\mu}{l_s\theta_{micro}}\left[\theta_{micro}U_{cl}\,F(\theta_{micro}) - \frac{J\,G(\theta_{micro})}{\rho_l}\right]. \tag{2.46}$$

https://doi.org/10.1017/jfm.2022.725 Published online by Cambridge University Press

The T^i derivative can be obtained from (2.40) by developing T^i into the Taylor series around $s = 0$:

$$\frac{\partial T^i}{\partial s} = -\frac{\mathcal{L}\theta_{micro}}{k} J. \tag{2.47}$$

Its substitution into (2.46) results in the expression

$$s\frac{\partial \Delta p}{\partial s} = \frac{\mu}{l_s \theta_{micro}} \left[U_{cl} F(\theta_{micro}) - J \left(\frac{G(\theta_{micro})}{\theta_{micro}\rho_l} + \frac{l_s \mathcal{L}\theta_{micro}}{\mu k} \gamma \right) \right]. \tag{2.48}$$

By combining (2.45) and (2.48), one obtains a differential equation for Δp that is valid asymptotically. Its solution (Janeček & Nikolayev 2012) shows that both Δp and J remain finite at the CL. The left-hand side of (2.48) thus tends to zero as $s \to 0$, which results in

$$J(s \to 0) = \frac{U_{cl} F(\theta_{micro})}{\dfrac{G(\theta_{micro})}{\theta_{micro}\rho_l} + \dfrac{l_s \mathcal{L}\theta_{micro}}{\mu k} \gamma}. \tag{2.49}$$

The pressure value at the CL is obtained easily by substituting (2.49) into (2.45). One can see that the pressure and mass flux are finite at the CL. However, a weaker form of the fourth boundary condition

$$\left. \frac{\partial \Delta p}{\partial s} \right|_{s \to 0} = 0 \tag{2.50}$$

is more convenient (Zhang & Nikolayev 2021) to provide a better numerical stability.

Another equation is needed to determine the CL speed (which is a part of the problem); (2.49) can be used for this purpose.

3. Results and discussion

The problem is solved numerically using the finite volume method (in this one-dimensional case, a finite volume is simply a line segment), which provides a better numerical stability than the conventional finite difference method. The numerical algorithm is similar to that used by Nikolayev (2010) and Zhang & Nikolayev (2021). The variables and their even-order derivatives are defined at the mesh nodes (the centres of segments), while the odd-order derivatives are defined at the segment boundaries. In order to capture the nanoscale effects without increasing significantly the total number of nodes, the meshing is exponentially refined near the CL. The nonlinear terms are managed with iterations.

The numerical approach is first tested for the adiabatic case against the asymptotic theory of Snoeijer & Eggers (2010). We then analyse the dewetting dynamics in the presence of liquid film evaporation. The numerical results are finally compared with the experimental data of Fourgeaud *et al.* (2016).

3.1. *Adiabatic dewetting*

A typical numerical result demonstrating the growth of the dewetting ridge under classical adiabatic conditions ($\Delta T = 0$) is shown in figure 4(*a*) for $\theta_{micro} = 10^\circ$ and for FC72 (more precisely, n-perfluorohexane) fluid, whose properties are listed in table 2. The flat part of the liquid film has constant thickness $h_\infty = 50\,\mu\text{m}$, which is a typical film thickness in the pulsating heat pipes (Nikolayev 2021). The moving CL has been chosen as the frame

https://doi.org/10.1017/jfm.2022.725 Published online by Cambridge University Press

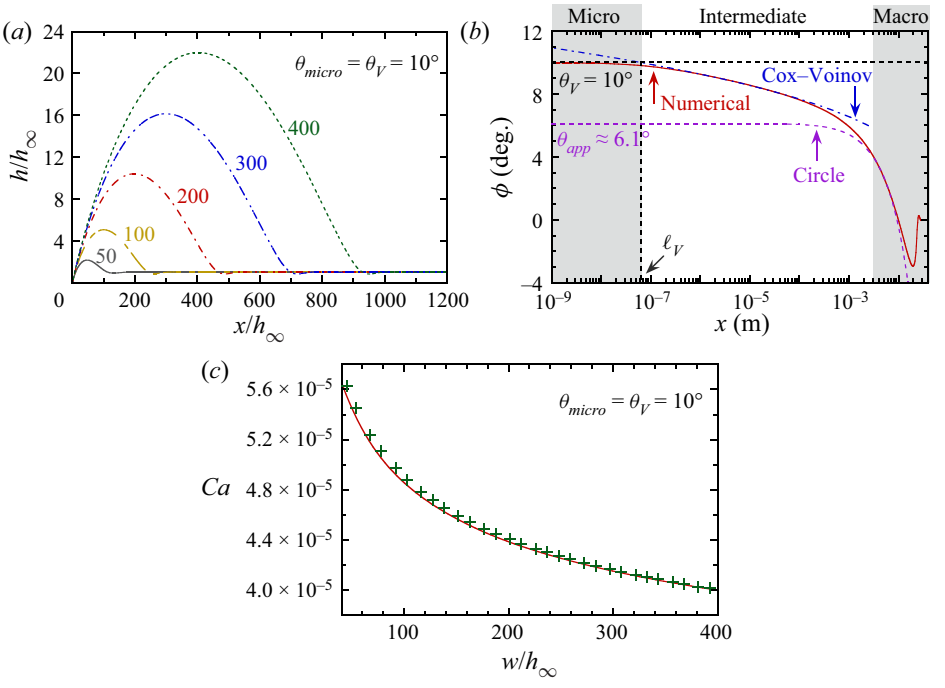


Figure 4. Numerical results concerning the adiabatic dewetting ($\Delta T = 0$) for $\theta_{micro} = 10°$ and $h_\infty = 50\,\mu$m. (*a*) Growth of the liquid ridge (see the supplementary movie). The curve parameter is w/h_∞. (*b*) Interface slope for $w/h_\infty = 200$. (*c*) Contact line receding speed Ca as a function of the ridge width. Line indicates numerical result; crosses come from (2.19).

of reference. Therefore, the CL stays at the origin. The ridge half-width w grows with time (see the supplementary movie available at https://doi.org/10.1017/jfm.2022.725), so the evolution is discussed in terms of w rather than time to enable a comparison with the multiscale theory.

The numerically obtained spatial variation of the interface slope ϕ is shown in figure 4(*b*) for the time moment at which $w/h_\infty = 200$ and $Ca = 4.39 \times 10^{-5}$ (red solid line). All three scales discussed in § 2.3 can be recognised.

The intermediate region obeys the governing equation (2.23). Its solution is known to be well approximated by the Cox–Voinov law (2.16). Since the (2.23) is of second order with respect to ϕ, its solution contains two integration constants: θ and ℓ_V. Obviously, in the absence of CL motion, the interface is straight, so $\phi(Ca = 0) = \theta_{micro}$, which results in $\theta = \theta_{micro}$. From the definition of the Voinov angle, $\theta_V = \theta_{micro}$ for the adiabatic case, and it remains nearly constant in a region that can be identified with the microregion.

The value $\ell_V \simeq 64$ nm is determined from fitting (2.16) to the numerical curve as an abscissa of the intersection of the fitting curve with the horizontal line $\phi = \theta_{micro}$. In agreement with the hypothesis of Fourgeaud *et al.* (2016), the ℓ_V value coincides with that given by the hydrodynamic slip: (2.18) results in $\ell_{Vsa} \simeq 63$ nm. This is not surprising as it exceeds the value provided by the Kelvin effect: $\ell_{VK} \simeq 38$ nm according to (3.2). This conclusion conforms to the discussion in § 2.4. One needs to note that during the ridge evolution, ℓ_V grows slightly with w/h_∞ (i.e. decreases with Ca), but the variation is below 3 %. This means that the Cox–Voinov formula is fairly accurate and is thus suitable for multiscale modelling.

https://doi.org/10.1017/jfm.2022.725 Published online by Cambridge University Press

https://doi.org/10.1017/jfm.2022.725 Published online by Cambridge University Press

	T_{sat} (K)	ρ_l (kg m^{-3})	ρ_v (kg m^{-3})	$\mathcal{L}$ (kJ kg^{-1})	k (W m^{-1} K^{-1})	μ (μPa s)	σ (N m^{-1})	γ (N m^{-1} K^{-1})	R^i (m^2 K W^{-1})
FC72	309.1	1668.5	6.193	89.536	0.0566	559.64	1.035×10^{-2}	7.5×10^{-5}	6.78×10^{-7}
Ethanol	318.15	768.04	0.4089	898.8	0.161	752.54	1.926×10^{-2}	1.24×10^{-4}	2.89×10^{-7}
Water	373.12	958.37	0.5977	2256.5	0.6791	281.66	5.892×10^{-2}	1.925×10^{-4}	6.37×10^{-8}

Table 2. Liquid properties at the selected saturation points.

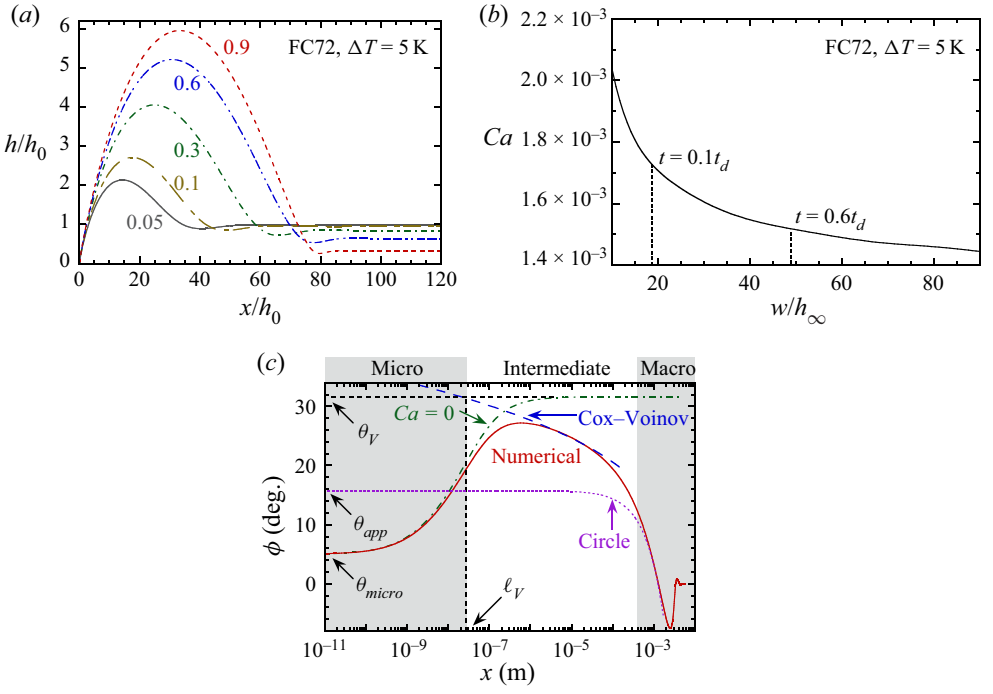


Figure 5. Numerical results showing the formation of a dewetting ridge for FC72; $\Delta T = 5$ K, $\theta_{micro} = 5^\circ$ and $h_0 = 50\,\mu$m. (*a*) Growth of the liquid ridge. The curve parameter is t/t_d. (*b*) Evolution of the contact line receding speed Ca. (*c*) Interface slope variation for $Ca = 1.614 \times 10^{-3}$.

As mentioned above, the liquid ridge is of circular shape in the macroregion. The corresponding fit is also plotted in figure 4(*b*) (violet dashed line). The angle at which this circle intersects the solid surface (i.e. the intersection of the fitting curve with the ordinate axis) defines the apparent contact angle $\theta_{app} \simeq 6.1^\circ$. The half-width w of the ridge can be obtained easily from the fit as a distance between the apparent CL and the ridge summit (figure 1).

The CL receding speed is not rigorously constant but decreases slowly. By using w and ℓ_V, both obtained from the numerical curve as discussed above, one can compare the numerical Ca to the asymptotic result (2.19) (figure 4*c*). The agreement is excellent, which shows the validity of the approach that we use.

3.2. *Dewetting at evaporation*

This subsection considers the liquid film evaporation caused by substrate heating. Three different fluids common for heat transfer applications are used in the calculations, whose properties are summarised in table 2. Initially, the liquid film has the thickness $h_0 = 50\,\mu$m typical for the pulsating heat pipe used by Fourgeaud *et al.* (2016) in their experiments.

Similarly to the adiabatic case, figure 5(*a*) demonstrates the dewetting ridge evolution at evaporation. The fluid is FC72 with $\theta_{micro} = 5^\circ$, and the substrate superheating is $\Delta T = 5$ K. Because of evaporation, liquid film thinning occurs, which is clearly visible in the flat film portion. The receding speed Ca decreases with time. It is shown in figure 5(*b*) as a function of the ridge half-width w (that increases with time similarly to the adiabatic case).

https://doi.org/10.1017/jfm.2022.725 Published online by Cambridge University Press

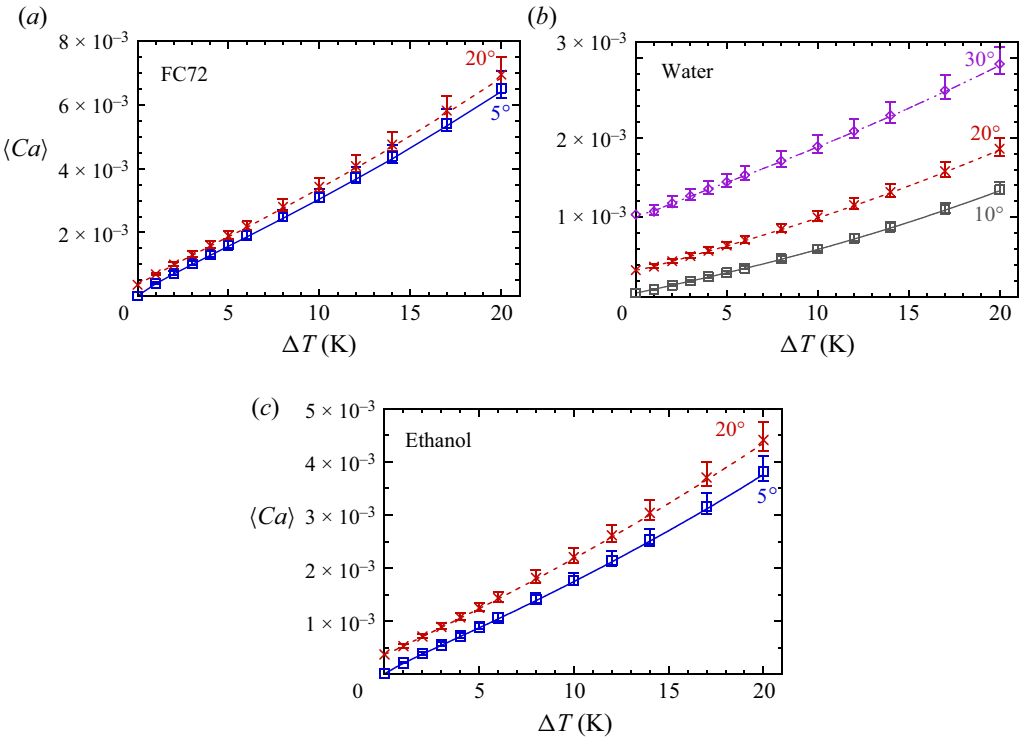


Figure 6. Comparison of numerical (characters with error bars) and theoretical (lines) results for $Ca(\Delta T)$ for several θ_{micro} and different fluids.

The central question of the dewetting theory concerns CL dynamics, i.e. Ca as a function of ΔT. However, during the film evolution, Ca decreases with time as shown in figure 5(*b*). For applications (e.g. in pulsating heat pipe modelling), one usually needs only an average speed. As the time evolution is slow, Ca can be averaged over a time interval; such an averaging is denoted hereafter with angle brackets. A practical averaging time interval needs to be chosen. Evidently, the averaging makes little sense for times close to t_d, near which the film evaporates completely. We choose the upper averaging limit to be $0.6t_d$. The averaging needs to be started at a time moment where the influence of initial conditions fades out; $0.1t_d$ is selected as the lower averaging limit. For the case of figure 5(*b*), $\langle Ca\rangle \simeq 1.60 \times 10^{-3}$. Repeating the process for different ΔT ranging from 0 to 20 K, we plot $\langle Ca\rangle$ as a function of ΔT in figure 6 (as characters with error bars) for several typical θ_{micro} values and for selected fluids. The upper and lower bounds of the error bars correspond to the numerical Ca at $t = 0.1t_d$ and $0.6t_d$, respectively. The error bars are narrower for small θ_{micro} and ΔT, because the speed variation is less drastic.

Note that the dewetting is not only accelerated by the evaporation; it can also be induced by evaporation (Fourgeaud *et al.* 2016). This is seen clearly in figure 6. For small θ_{micro} (i.e. for conditions of almost complete wetting), the adiabatic dewetting speed is extremely low, which means no dewetting in practice. However, it grows considerably with superheating.

3.3. *Comparison to multiscale theory*

A full numerical solution of the dewetting problem is, however, time- and resource-consuming because of the necessity to resolve several very different length scales

https://doi.org/10.1017/jfm.2022.725 Published online by Cambridge University Press

on the one hand, and to iterate to find CL speed at each time moment, on the other. For this reason, the multiscale approach to this problem can be a viable alternative. Let us compare the numerical result and the solutions computed in each of the regions within the multiscale approach to determine if it holds.

Figure 5(*c*) shows the spatial variation of the interface slope at the time moment $t = 0.33t_d$. Note the extent of the solution over multiple decades, which it was possible to compute thanks to the mesh refinement near the CL. Similarly to the adiabatic case, three regions can be identified clearly. First, we perform the numerical matching of the microscopic and intermediate regions.

As discussed in § 2.3, the microregion-governing equation can be obtained by neglecting both the transient and the U_{cl}-containing terms in (2.39), which thus reduces to (Janeček & Nikolayev 2014)

$$\frac{\partial}{\partial s}\left\{\frac{1}{\mu\, G(\phi)}\left[\frac{\zeta}{2}\,(\zeta + 2l_s)\,\frac{\partial \sigma}{\partial s} + \frac{\zeta^2}{3}\,(\zeta + 3l_s)\,\frac{\partial \Delta p}{\partial s}\right]\right\} = -\frac{J}{\rho_l}. \tag{3.1}$$

This corresponds to the problem of an evaporating immobile liquid wedge sketched in figure 2(*a*). The boundary condition $K = 0$ is applied at the right-hand end of the integration interval (which corresponds to the constant slope at infinity) instead of (2.42). The other three boundary conditions (see (2.44) and (2.50)) are defined at the CL and thus remain valid.

The slope variation corresponding to the microregion solution is shown in figure 5(*c*) (green dash-dotted line). It exhibits the ϕ saturation at large x to the value $\theta_V \simeq 31.65^\circ$. The abscissa axis is extended to non-physically small values to show the $x \to 0$ convergence to θ_{micro}.

The treatment of the intermediate and macroscopic regions is similar to the adiabatic case considered in § 3.1. The fit (blue dashed line in figure 5*c*) to the Cox–Voinov law (2.16) with $\theta = \theta_V$ results in $\ell_V \simeq 20$ nm for this particular case. The fit to a circle in the macroregion (violet dotted line in figure 5*c*) gives $\theta_{app} \simeq 15.7^\circ$.

By repeating the fitting for different ΔT ranging from 0 to 20 K and for three selected fluids, one obtains figure 7, which demonstrates θ_V and $\langle\theta_{app}\rangle$ as functions of ΔT for different fluids. As θ_{app} increases slowly with time as the ridge grows, an average value $\langle\theta_{app}\rangle$ is taken over the course $(0.1t_d, 0.6t_d)$. Here, θ_V increases monotonically with ΔT as discussed in numerous works on the microregion (see Nikolayev (2022) for a review); $\theta_V(\Delta T = 0) = \theta_{micro}$.

The Voinov length ℓ_V obtained from the Cox–Voinov fit depends on time but its variation is extremely weak, of the order of the fitting error (less than 2 %). We plot ℓ_V as a function of ΔT in figure 8 for different fluids. As expected for the microregion scale, ℓ_V is of the order of 10–100 nm. It shrinks monotonically with ΔT.

One can now use the multiscale theoretical prediction (2.17) to compare with the numerical data. The averaged values of all parameters obtained from the numerical calculation (such as $\langle w\rangle$ and $\langle Ca\rangle$) can be used on the right-hand side of (2.17). The resulting $\langle\theta_{app}\rangle$ is plotted as a function of ΔT as blue dotted lines for different fluids in figure 7. A good agreement with the numerical data for all the fluids indicates the success of the multiscale theory.

More importantly, it is possible to compare the numerics to the asymptotic theoretical result (2.19) for $\langle Ca\rangle$. The averaged values of all the parameters $\langle w\rangle$, $\langle h\rangle$, θ_V and ℓ_V obtained from the numerical calculation can be used in the right-hand side of (2.19). In figure 6, the lines show the theoretical results while the characters are the numerical data.

https://doi.org/10.1017/jfm.2022.725 Published online by Cambridge University Press

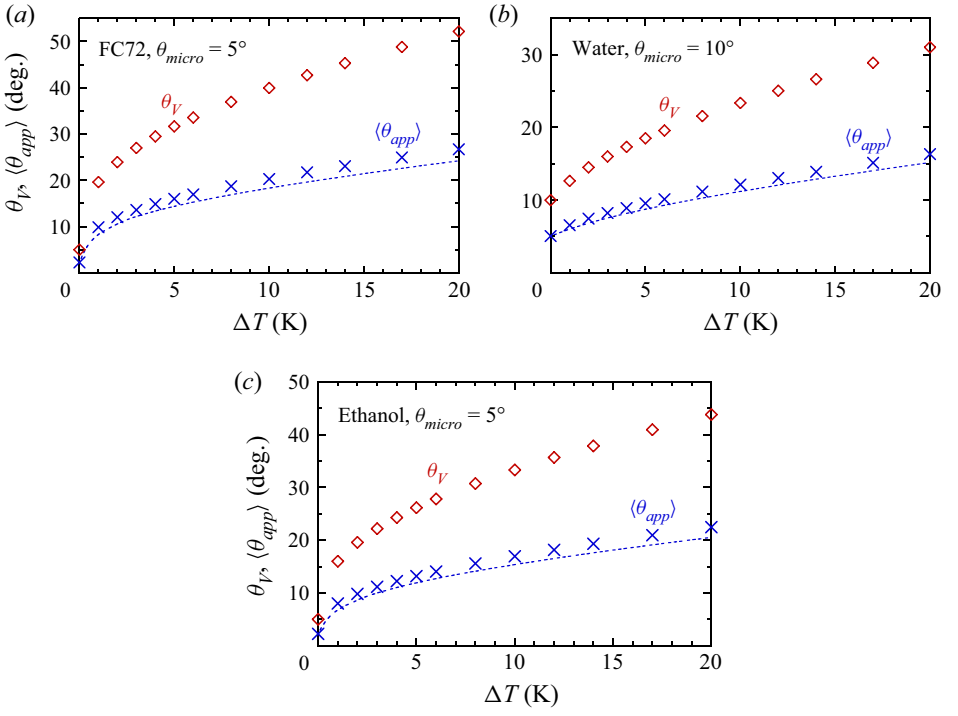


Figure 7. Values of θ_V (red diamonds) and $\langle\theta_{app}\rangle$ (blue crosses) as functions of ΔT for different fluids. The numerical data are shown with characters, while the blue dotted line corresponds to the multiscale theory result for $\langle\theta_{app}\rangle$.

Again, the agreement is excellent. One concludes that the multiscale theory is valid for the evaporation case.

3.4. *Voinov length approximation*

Two key parameters engendering from the microregion enter (2.19): θ_V and ℓ_V. While the first parameter θ_V of the multiscale theory is relatively easy to obtain as it requires solving only the microregion problem, the second parameter ℓ_V is a more delicate issue. To avoid the laborious numerical calculation of ℓ_V for a particular fluid and ΔT, a simpler approach is desirable.

In the case of phase change, if only the Kelvin effect is included, then one finds a general expression for the Voinov length (Janeček *et al.* 2013)

$$\ell_{VK} \simeq f(\epsilon)\,\frac{\sqrt{3\mu k T_{sat}}}{\theta_V^2 \rho_l \mathcal{L}}, \tag{3.2}$$

where

$$\epsilon = \frac{\sqrt{3\mu k T_{sat}}}{\sigma\theta_V^3}\,\frac{\Delta T}{T_{sat}}, \tag{3.3}$$

and $f(\epsilon)$ is an increasing function shown in figure 3(*b*) of Janeček *et al.* (2013); for positive ΔT, it varies between $f(0) \simeq 1.31$ and $f(\epsilon_c) \simeq 3.02$. Note that for large ΔT, ϵ tends to a critical value $\epsilon_c \simeq 0.3$, which results in $\theta_V \sim \Delta T^{1/3}$.

https://doi.org/10.1017/jfm.2022.725 Published online by Cambridge University Press

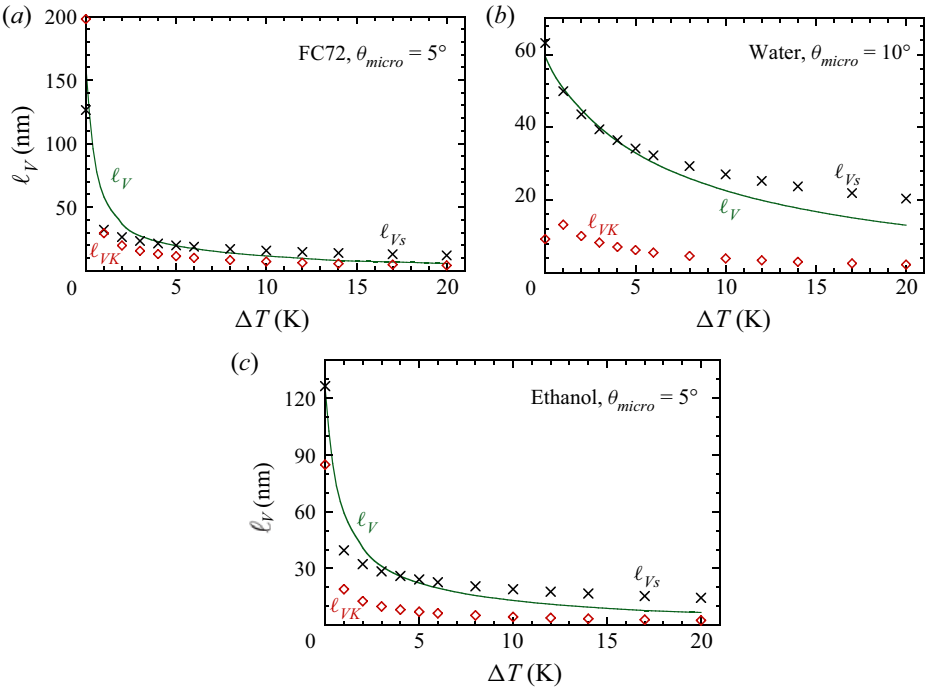


Figure 8. Numerically obtained variation of ℓ_V with ΔT (lines) for different fluids. The variations of ℓ_{VK} (diamonds) and ℓ_{Vs} (crosses) are also shown. The value of ℓ_{Vsa} from (2.18) corresponds to $\ell_{Vs}(\Delta T = 0)$.

However, because other nanoscale effects have been accounted for in the calculation, figure 8 shows that, at least for conventional fluids, this value ℓ_{VK} remains much smaller than the numerical result and is thus hardly suitable in practice.

The slip-controlled value ℓ_{Vsa} (2.18) that was used by Fourgeaud *et al.* (2016) for ℓ_V is known only for $\Delta T = 0$. Its value can be somewhat larger than the numerical ℓ_V for $\Delta T \neq 0$ (figure 8), so one needs a better general expression. On the basis of the scaling discussed in § 2.4, the slip should have a major impact on ℓ_V. Therefore, we propose to use for ℓ_V the expression

$$\ell_{Vs} = \frac{3l_s}{e\theta_V}. \tag{3.4}$$

Figure 8 shows that the quality of this approximation is satisfactory, especially accounting for the fact that ℓ_V always appears under the logarithm in (2.17) and (2.19).

3.5. *Comparison with experiment*

The only experiment on the dewetting at evaporation, which comprises the data on both θ_{app} and Ca, and with which we can thus compare our modelling, was conducted by Fourgeaud *et al.* (2016). They have observed the dewetting of an ethanol film on a heated sapphire substrate, in an airtight chamber filled with the saturated ethanol vapour. Initially, an ethanol film of thickness $\sim 60\,\mu$m was deposited on the solid surface, whose temperature was above the saturation temperature of the vapour. Both substrate dewetting and liquid film thinning were observed. The time evolution of the interface profile (including CL position, w and h_∞) and the vapour pressure were recorded.

https://doi.org/10.1017/jfm.2022.725 Published online by Cambridge University Press

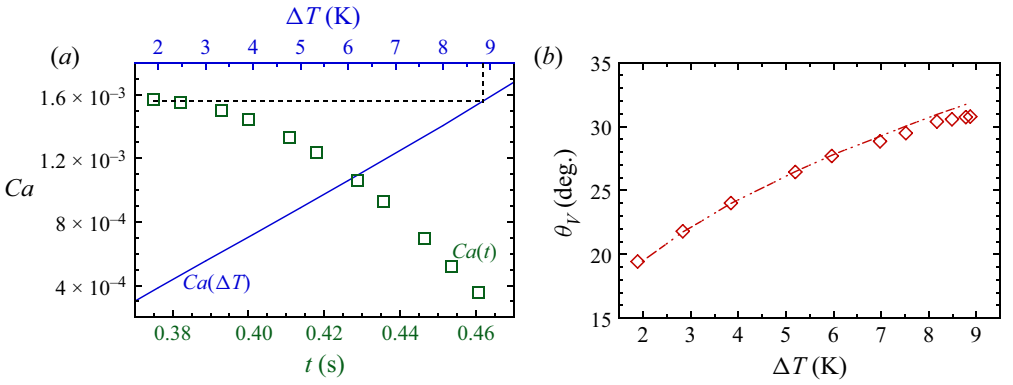


Figure 9. (*a*) Experimental data of Fourgeaud *et al.* (2016) for $Ca(t)$ (green squares plotted with respect to the lower abscissa axis) and numerical curve $Ca(\Delta T)$ (blue line plotted with respect to the upper abscissa axis). (*b*) Comparison of $\theta_V(\Delta T)$ functions obtained with the experimental data (Fourgeaud *et al.* 2016) (red diamonds) and the numerical calculation (line).

Hence CL speed could be derived. Here, T_{sat} was found with the vapour pressure. The value of θ_{app} was obtained by fitting the liquid ridge profile to a circle, whose intersection with the solid surface gave θ_{app}, similarly to our numerical procedure. The substrate temperature T_w could not be measured, but it was clear that it remained nearly constant because of the large thermal inertia of the substrate. The superheating $\Delta T = T_w - T_{sat}$ varied because of strong T_{sat} variation. According to the assumption of Fourgeaud *et al.* (2016), $T_w = 48°\text{C}$. In the present work, we propose another approach. Instead of assuming a T_w value, we calculate ΔT for each data point from the experimental Ca by using the numerical $Ca(\Delta T)$ curve for ethanol (figure 6*c*). The calculation is done for $\theta_{micro} = 5°$, which is the value found originally by Fourgeaud *et al.* (2016).

Figure 9(*a*) plots the experimental data for $Ca(t)$ (green squares) and the numerical curve $Ca(\Delta T)$ (blue solid line, the same as in figure 6*c*). By placing the experimental Ca value to the numerical curve, one recovers ΔT for each experimental point. For instance, for the first data point at $t = 0.375\,\text{s}$, given $Ca \simeq 1.57 \times 10^{-3}$, one recovers $\Delta T \simeq 8.9\,\text{K}$.

In the next step, ℓ_V can be computed from the numerical curve $\ell_V(\Delta T)$ (figure 8*c*). Finally, one can calculate θ_V with (2.17) by using the experimental data for θ_{app} and w and the ℓ_V found before. We note that the latter has only a small impact on the result as it enters under the logarithm. The points $(\Delta T, \theta_V)$ obtained in this way are plotted in figure 9(*b*) as red diamonds. As demonstrated in figure 7, θ_V can also be obtained numerically as a function of ΔT. The corresponding dependence is plotted as the red curve in figure 9(*b*), the same as the diamonds in figure 7(*c*). The numerical line agrees with the experimental estimations, which shows the validity of our numerical approach.

We should also verify that $T_w = T_{sat} + \Delta T$ remains nearly constant for all data points. From our ΔT evaluation, $T_w = 42.7 \pm 0.4\,°\text{C}$. Such a value is a plausible estimation of T_w. In their original work, Fourgeaud *et al.* (2016) obtained a difference of $\simeq 14\%$ between the theoretical and experimental Ca values. We can see now that this difference can be attributed to their overestimation of T_w.

4. Conclusions

The dewetting dynamics in the presence of the liquid film evaporation is analysed for the case where the liquid film is in contact with the pure vapour of the same fluid. To increase

https://doi.org/10.1017/jfm.2022.725 Published online by Cambridge University Press

the precision of numerical results at an interface slope higher than the conventional lubrication theory can handle, we develop the generalised lubrication theory (which uses, however, phenomenological arguments yet to be verified). Several nanoscale effects are included to produce realistic results: hydrodynamic slip, interfacial thermal resistance, Kelvin and Marangoni effects, and the vapour recoil. The relative importance of all these effects is analysed. Our scaling analysis shows that, in general, none of the above nanoscale effects should be neglected while evaluating the evaporation impact. The Kelvin effect, while being less important in terms of its magnitude, is needed to provide the finiteness of liquid pressure at the contact line. Our theoretical description leads to the contact line receding phenomenon accompanied by the spontaneous liquid evaporation in its close vicinity. The evaporation rate at the contact line conforms to its speed. In the presence of the forced evaporation caused by substrate heating, the dewetting accelerates. The results show that the dewetting phenomenon is not only accelerated at evaporation; the dewetting can also be induced by evaporation. The dependence of the dewetting speed on the substrate superheating has been computed for three fluids (FC72, ethanol and water) for different wetting conditions. Unfortunately, it is difficult at this stage to introduce an analytical theory showing the importance of the boosting effect of evaporation because of a large number of effects that contribute to it.

The model has been validated against the asymptotic multiscale theory of dewetting developed by Snoeijer & Eggers (2010) for adiabatic conditions. The multiscale theory has been generalised to the evaporation case. It results in a simple analytical expression for the dewetting speed. The main parameters of this expression are the Voinov length and the Voinov angle (the interface slope formed in the microregion), through which the nanoscale effects impact the macroscale physics. While the Voinov angle is relatively easy to compute (it requires only a solution of a stationary microregion model mastered by many research groups), the Voinov length requires a more sophisticated calculation. An approximate analytical formula for the Voinov length is proposed. The results of the generalised multiscale model agree with the numerical calculations. It is shown that the evaporative mass loss at the contact line (hypothesised by Fourgeaud *et al.* 2016) does not lead to any additional acceleration of its motion controlled entirely by capillarity and by the evaporation-driven modification of the Voinov angle.

The numerical results have been compared to the experiment of Fourgeaud *et al.* (2016). For this, their experimental data were reanalysed, and good agreement with our numerics was achieved.

This study's results are of importance for many applications such as bubble growth in boiling (in particular, the microlayer dynamics; Tecchio *et al.* 2022) and pulsating heat pipes, where the liquid film dynamics crucially affects the overall heat exchange.

Supplementary movie. A supplementary movie is available at https://doi.org/10.1017/jfm.2022.725.

Funding. The present work is supported by the project TOPDESS, financed through the Microgravity Application Programme by the European Space Agency. This paper is also a part of the PhD thesis of X.Z. co-financed by the CNES and the CEA NUMERICS programme, which has received funding from the European Union Horizon 2020 research and innovation programme under the Marie Skłodowska-Curie grant agreement no. 800945. Additional financial support of CNES awarded through GdR MFA is acknowledged.

Declaration of interests. The authors report no conflict of interest.

Author ORCIDs.
Xiaolong Zhang https://orcid.org/0000-0002-7920-3876;
Vadim S. Nikolayev https://orcid.org/0000-0002-9486-746X.

https://doi.org/10.1017/jfm.2022.725 Published online by Cambridge University Press

Appendix A. Stokes problems in the straight wedge

In the polar reference (r, φ) (figure 3*b*), the components of the liquid velocity $\boldsymbol{u} = (u_r, u_\varphi)$ can be expressed as

$$\left.\begin{aligned} u_r &= \frac{1}{r}\frac{\partial \Psi}{\partial \varphi}, \\ u_\varphi &= -\frac{\partial \Psi}{\partial r}. \end{aligned}\right\} \tag{A1}$$

with the stream function Ψ that satisfies the equation

$$\nabla^4 \Psi = 0. \tag{A2}$$

Because of the mass conservation along the wedge in both problems considered below, the liquid flux Φ defined by (2.30) is independent of r.

A.1. *Liquid flow created by contact line motion*

Consider the substrate moving with speed U_{cl} to the left in figure 3(*b*), which is equivalent to the CL receding. The boundary conditions to (A2) are

$$\left.\begin{aligned} &\frac{\partial \Psi}{\partial \varphi} = -rU_{cl} \quad \text{and} \quad \frac{\partial \Psi}{\partial r} = 0 \quad \text{at } \varphi = 0, \\ &\frac{\partial \Psi}{\partial r} = 0 \quad \text{and} \quad \frac{\partial^2 \Psi}{\partial \varphi^2} = 0 \quad \text{at } \varphi = \phi. \end{aligned}\right\} \tag{A3}$$

The solution to this problem is (Moffatt 1964)

$$\Psi(r, \varphi) = -rU_{cl}\,\frac{(2\phi - \varphi)\sin\varphi - \varphi\sin(2\phi - \varphi)}{2\phi - \sin(2\phi)}, \tag{A4}$$

and the pressure gradient at the interface reads

$$\frac{\partial p_l}{\partial r} = U_{cl}\,\frac{\mu}{r^2}\,\frac{4\sin\phi}{\sin(2\phi) - 2\phi}, \tag{A5}$$

which is equivalent to (2.23) accounting for (2.26).

Note that $\Phi = 0$ for this case as it is zero in the apex. Many authors pointed out the non-integrable pressure divergence $p \sim r^{-2}$. This means the infinite viscous dissipation, so such a problem statement is in fact non-physical, and other microscale phenomena like the hydrodynamic slip and/or the Kelvin effect need to be accounted for to relax the singularity.

A.2. *Liquid flow created by localised evaporation*

Consider the flow induced by a the localised evaporation modelled by a point source Φ placed at the wedge apex (figure 3*b*). The boundary conditions to (A2) are

$$\left.\begin{aligned} &\frac{\partial \Psi}{\partial \varphi} = 0 \quad \text{and} \quad \frac{\partial \Psi}{\partial r} = 0 \quad \text{at } \varphi = 0, \\ &\frac{\partial \Psi}{\partial r} = 0 \quad \text{and} \quad \frac{\partial^2 \Psi}{\partial \varphi^2} = 0 \quad \text{at } \varphi = \phi. \end{aligned}\right\} \tag{A6}$$

They signify (i) the impermeability and no-slip conditions at the solid surface $\varphi = 0$, and (ii) the impermeability and zero tangential stress at the liquid–vapour interface $\varphi = \phi$.

https://doi.org/10.1017/jfm.2022.725 Published online by Cambridge University Press

The velocity should satisfy (2.30), where Φ is constant. One mentions that for this, $\Psi(r, \varphi)$ should be independent of r.

The solution found by Mathieu (2003) is

$$\Psi(r, \varphi) = \Phi \frac{\sin(2\phi - 2\varphi) + 2\varphi\cos(2\phi)}{2\phi\cos(2\phi) - \sin(2\phi)}. \tag{A7}$$

The corresponding pressure field is

$$p_l(r, \varphi) = \Phi \frac{\mu}{r^2} \frac{4\cos(2\phi - 2\varphi)}{\sin(2\phi) - 2\phi\cos(2\phi)}, \tag{A8}$$

and the pressure gradient at the interface $\varphi = \phi$ reads

$$\frac{\partial p_l}{\partial r} = \Phi \frac{\mu}{r^3} \frac{4}{\phi\cos(2\phi) - \cos\phi\sin\phi}, \tag{A9}$$

which is equivalent to (2.31) with $l_s = 0$.

Appendix B. Characteristic length scales in the microregion

The characteristic lengths shown in table 1 can be obtained from (2.13)–(2.15) and (3.1) describing the microregion. For these estimations, small slopes are assumed, so $G \simeq 1$ and $\zeta \simeq h$. One assumes for the estimation the wedge liquid shape with the opening angle θ. Therefore, if one denotes the x scale as ℓ (to be defined for each effect), then the h scale is $\theta\ell$. One finds from (2.4) that $K \sim \theta/\ell$, so $\Delta p \sim \sigma K \sim \sigma\theta/\ell$. The mass flux scales as $J \sim k\,\Delta T/(\mathcal{L}\theta\ell)$. From (2.10), one finds the interfacial resistance scale $\ell_R = R^i k/\theta$. From (2.13), one finds the vapour recoil scale ℓ_r. It reflects the vapour recoil on the Voinov angle. The slip length scale ℓ_s is easily found from (3.1). The Kelvin length scale ℓ_K is derived by Janeček *et al.* (2013).

The Marangoni effect is more delicate because the T^i spatial variation does not appear without either Kelvin or interface resistance terms; cf. (2.9). After having left aside the slip, (3.1) reduces to

$$\frac{1}{\mu}\frac{\partial}{\partial x}\left[-\frac{\gamma h^2}{2}R^i\mathcal{L}\frac{\partial J}{\partial x} + \left(\frac{h^3}{3} - \frac{\gamma h^2}{2}\frac{T_{sat}}{\mathcal{L}\rho_l}\right)\frac{\partial \Delta p}{\partial x}\right] = -\frac{J}{\rho_l}. \tag{B1}$$

By comparing the two terms in the round brackets (the second of which comes from the Kelvin effect), one obtains the Marangoni–Kelvin scale

$$\ell_{MK} = \frac{3\gamma T_{sat}}{2\theta\mathcal{L}\rho_l}. \tag{B2}$$

It appears to be below 1 nm for all the cases under consideration, so the corresponding effect is negligible. Conversely, the Marangoni effect appearing due to the interfacial thermal resistance with respect to the capillary action is characterised by the balance of the terms

$$\frac{\gamma h^2}{2}R^i\mathcal{L}\frac{\partial J}{\partial x} \quad \text{and} \quad \frac{h^3}{3}\frac{\partial \Delta p}{\partial x}, \tag{B3a,b}$$

which results in the characteristic scale

$$\ell_{MR} = \frac{3\gamma\,\Delta T\,R^i k}{2\theta^3\sigma} = \frac{3\gamma\,\Delta T}{2\theta^2\sigma}\ell_R \tag{B4}$$

displayed in table 1.

https://doi.org/10.1017/jfm.2022.725 Published online by Cambridge University Press

Since the interfacial resistance should be present to provide the Marangoni effect, one should check if a range of x exists such that $\ell_R < x < \ell_{MR}$ (i.e. where the Marangoni effect created by the interfacial resistance is more important than the effect of the interfacial resistance alone). This interval exists if

$$\ell_R < \ell_{MR}, \tag{B5}$$

equivalent to

$$\gamma\, \Delta T > \tfrac{2}{3}\, \theta^2 \sigma. \tag{B6}$$

This means that ℓ_{MR} is relevant if the product $\gamma\, \Delta T$ is large enough.

References

Anderson, D.M., Cermelli, P., Fried, E., Gurtin, M.E. & McFadden, G.B. 2007 General dynamical sharp-interface conditions for phase transformations in viscous heat-conducting fluids. *J. Fluid Mech.* **581**, 323–370.

Anderson, D.M. & Davis, S.H. 1994 Local fluid and heat flow near contact lines. *J. Fluid Mech.* **268**, 231–265.

Anderson, D.M. & Janeček, V. 2018 Comment on L. M. Hocking, 'On contact angles in evaporating liquids' [*Phys. Fluids* **7**, 2950–2955 (1995)]. *Phys. Fluids* **30** (7), 079101.

Boender, W., Chesters, A.K. & van der Zanden, A.J.J. 1991 An approximate analytical solution of the hydrodynamic problem associated with an advancing liquid–gas contact line. *Int. J. Multiphase Flow* **17**, 661–676.

Brochard-Wyart, F., Di Meglio, J.-M., Quere, D. & de Gennes, P.-G. 1991 Spreading of nonvolatile liquids in a continuum picture. *Langmuir* **7** (2), 335–338.

Bureš, L. & Sato, Y. 2021 On the modelling of the transition between contact-line and microlayer evaporation regimes in nucleate boiling. *J. Fluid Mech.* **916**, A53.

Chan, T.S., Kamal, C., Snoeijer, J.H., Sprittles, J.E. & Eggers, J. 2020 Cox–Voinov theory with slip. *J. Fluid Mech.* **900**, A8.

Chan, T.S., Srivastava, S., Marchand, A., Andreotti, B., Biferale, L., Toschi, F. & Snoeijer, J.H. 2013 Hydrodynamics of air entrainment by moving contact lines. *Phys. Fluids* **25** (7), 074105.

Cox, R.G. 1986 The dynamics of the spreading of liquids on a solid surface. *Part 1. Viscous flow. J. Fluid Mech.* **168**, 169–194.

Delon, G., Fermigier, M., Snoeijer, J.H. & Andreotti, B. 2008 Relaxation of a dewetting contact line. *Part 2: Experiments. J. Fluid Mech.* **604**, 55–75.

Edwards, A.M.J., Ledesma-Aguilar, R., Newton, M.I., Brown, C.V. & McHale, G. 2016 Not spreading in reverse: the dewetting of a liquid film into a single drop. *Sci. Adv.* **2** (9), e1600183.

Fourgeaud, L., Ercolani, E., Duplat, J., Gully, P. & Nikolayev, V.S. 2016 Evaporation-driven dewetting of a liquid film. *Phys. Rev. Fluids* **1** (4), 041901.

de Gennes, P.-G. 1985 Wetting: statics and dynamics. *Rev. Mod. Phys.* **57**, 827–863.

de Gennes, P.-G., Brochard-Wyart, F. & Quéré, D. 2004 *Capillarity and Wetting Phenomena: Drops, Bubbles, Pearls, Waves*. Springer.

Hocking, L.M. 1983 The spreading of a thin drop by gravity and capillarity. *Q. J. Mechanics Appl. Math.* **36** (1), 55–69.

Hocking, L.M. 1995 On contact angles in evaporating liquids. *Phys. Fluids* **7**, 2950–2955.

Janeček, V., Andreotti, B., Pražák, D., Bárta, T. & Nikolayev, V.S. 2013 Moving contact line of a volatile fluid. *Phys. Rev. E* **88** (6), 060404.

Janeček, V. & Nikolayev, V.S. 2012 Contact line singularity at partial wetting during evaporation driven by substrate heating. *Europhys. Lett.* **100** (1), 14003.

Janeček, V. & Nikolayev, V.S. 2014 Triggering the boiling crisis: a study of the dry spot spreading mechanism. *Interfacial Phenom. Heat Transf.* **2** (4), 363–383.

Lauga, E., Brenner, M.P. & Stone, H.A. 2007 Microfluidics: the no-slip boundary condition. In *Springer Handbook of Experimental Fluid Dynamics* (ed. C. Tropea, A. Yarin & J. Foss), chap. 19, pp. 1217–1240. Springer.

Mathieu, B. 2003 Etudes physiques, expérimentale et numérique des mécanismes de base intervenant dans les écoulements diphasiques. PhD thesis, Polytech Marseille, Université de Provence.

Moffatt, H.K. 1964 Viscous and resistive eddies near a sharp corner. *J. Fluid Mech.* **18** (1), 1–18.

https://doi.org/10.1017/jfm.2022.725 Published online by Cambridge University Press

NIKOLAYEV, V.S. 2010 Dynamics of the triple contact line on a nonisothermal heater at partial wetting. *Phys. Fluids* **22** (8), 082105.

NIKOLAYEV, V.S. 2021 Physical principles and state-of-the-art of modeling of the pulsating heat pipe: a review. *Appl. Therm. Eng.* **195**, 117111.

NIKOLAYEV, V.S. 2022 Evaporation effect on the contact angle and contact line dynamics. In *The Surface Wettability Effect on Phase Change* (ed. M. Marengo & J.D. Coninck), chap. 6, pp. 133–187. Springer.

NIKOLAYEV, V.S. & BEYSENS, D.A. 1999 Boiling crisis and non-equilibrium drying transition. *Europhys. Lett.* **47** (3), 345–351.

REDNIKOV, A. & COLINET, P. 2013 Singularity-free description of moving contact lines for volatile liquids. *Phys. Rev. E* **87** (1), 010401.

SAXTON, M.A., VELLA, D., WHITELEY, J.P. & OLIVER, J.M. 2017 Kinetic effects regularize the mass-flux singularity at the contact line of a thin evaporating drop. *J. Eng. Math.* **106** (1), 47–73.

SNOEIJER, J.H. 2006 Free-surface flows with large slopes: beyond lubrication theory. *Phys. Fluids* **18**, 021701.

SNOEIJER, J.H. & ANDREOTTI, B. 2013 Moving contact lines: scales, regimes, and dynamical transitions. *Annu. Rev. Fluid Mech.* **45** (1), 269–292.

SNOEIJER, J.H. & EGGERS, J. 2010 Asymptotic analysis of the dewetting rim. *Phys. Rev. E* **82** (5), 056314.

TECCHIO, C., ZHANG, X., CARITEAU, B., ZALCZER, G., ROCA I CABARROCAS, P., BULKIN, P., CHARLIAC, J., VASSANT, S. & NIKOLAYEV, V. 2022 Microlayer dynamics at bubble growth in boiling. In *Proc. 16th Int. Conf. Heat Transfer Fluid Mech. Thermodynamics (HEFAT-ATE 2022)*, pp. 624-629.

URBANO, A., TANGUY, S., HUBER, G. & COLIN, C. 2018 Direct numerical simulation of nucleate boiling in micro-layer regime. *Int. J. Heat Mass Transfer* **123**, 1128–1137.

VOINOV, O. 1976 Hydrodynamics of wetting. *Fluid Dyn.* **11** (5), 714–721.

WAYNER, P.C. 1993 Spreading of a liquid film with a finite contact angle by the evaporation/condensation process. *Langmuir* **9** (1), 294–299.

ZHANG, X. & NIKOLAYEV, V.S. 2021 Liquid film dynamics with immobile contact line during meniscus oscillation. *J. Fluid Mech.* **923**, A4.

https://doi.org/10.1017/jfm.2022.725 Published online by Cambridge University Press